View Article Online
DOI: 10.1039/C6RA12076H

Identifying the Preferred Interaction Mode of Naringin with Gold Nanoparticles through Experimental, DFT and TDDFT Techniques: Insights into their Sensing and Biological Applications

Baljinder Singh[$,a], Monika Rani[$,b], Janpreet Singh[a], Lovika Moudgil[a], Prateek Sharma[c], Sanjeev Kumar[c], G.S.S. Saini[a], S.K. Tripathi[a], Gurinder Singh[d] and Aman Kaura[d, *]

[a]*Department of Physics, Centre of Advanced Study in Physics, Panjab University, Chandigarh, 160014, India*
[b]*Centre for Nanoscience and Nanotechnology, Panjab University, Chandigarh, 160014, India*
[c]*Centre for Biosciences, Central University of Punjab, Bathinda, 151001, India*
[d]*Department of UIET, Panjab University SSG Regional Centre Hoshiarpur, Panjab, 146001, India*
** Corresponding author, Tel.: +91-9501911977, Fax: +91-1882-282221*
***Electronic mail:** amankaura1979@gmail.com; aman_kaura@yahoo.co.in
[$] First two authors have equal contribution

Abstract

In this work, binding behaviour of naringin-a flavonoid with AuNPs is explained by combining experimental and theoretical approach. We have systematically analysed the effect of temperature and concentration of naringin and gold (Au) in the formation of Naringin stabilized Au nanoparticles (N-AuNPs). The interaction of naringin with gold nanoparticles (AuNPs) is investigated by various techniques such as UV-Visible, TEM, FT-IR, XRD and gel electrophoresis. These studies indicate that naringin acts as reducing and stabilizing agent. Further, we have modelled the two side chains of naringin with the functional groups $[C_{10}H_7O_2]$ and $[C_6H_5O]^-$, identified the lowest energy configurations of these groups with AuNPs with the help of density functional theory (DFT). The $[C_{10}H_7O_2]$-Au_{13} has higher binding energy than $[C_6H_5O]^-$-Au_{13} and it is attributed to delocalized molecular orbitals in $[C_{10}H_7O_2]$, hence higher charge transfer to the Au_{13} cluster. On the basis of the resulting structures, we examine the optical properties using time-dependent density functional theory (TDDFT). We observe significant changes in the optical spectra of the representative structures of side chains with the AuNPs. The peak in spectra of Vis region of $[C_{10}H_7O_2]$-Au_{13} undergoes shift towards lower wavelength in comparison to $[C_6H_5O]^-$-Au_{13}. Natural transition orbitals (NTOs) of hole and particle states of $[C_{10}H_7O_2]$-Au_{13} conjugate system are localized on $[C_{10}H_7O_2]$ and Au_{13} respectively, whereas for the $[C_6H_5O]^-$-Au_{13} both hole and particle states are localized on the Au_{13} cluster. These N-AuNPs show their applicability as a sensor for detecting aluminium ions (Al^{3+}) in aqueous solution. These NPs are also found to be biocompatible with normal red blood

View Article Online
DOI: 10.1039/C6RA12076H

cells and MDAMB-231 breast carcinoma cell lines, as evaluated from hemolysis and cytotoxicity assays. Thus, naringin offers non-toxic and bio friendly N-AuNPs, which are considered to be the best vehicle for drug release and other possible biomedical and sensing applications.

View Article Online
DOI: 10.1039/C6RA12076H

Introduction

Flavonoids are a group of widely distributed products which are found in plants, fruits, vegetables, nuts, seeds as well as in spices [1-3]. They exhibit a range of biological and pharmacological activities such as antimicrobial [4], antioxidant [5], antiviral [6], antitumor [7] anti-inflammatory [1], antivirus [8], anti-allergic [9] etc. Such beneficial properties are attributed to the presence of poly phenolic groups in these molecules, which are known to scavenge free radicals, chelate metal ions, activate antioxidant enzymes and inhibit certain enzyme systems [10]. In particular, naringin (Figure SI-1a, Supporting Information) is the predominant flavonoid in grape fruit and many citrus herbs as well. A variety of other pharmacological effects have been observed in vitro or in animal studies [14-16], but their specific relevance to human health is unknown.

On the other hand, there is significant interest in investigating the therapeutic potential of AuNPs as it bridges the gap between nano technology and therapy. Among different synthetic routes to nanoparticle formation, bioinspired methods are considered better compared to chemical routes because these avoid the use of toxic chemicals [17-19]. The phytochemicals mainly flavonoids and phenolic compounds, possess strong reducing properties [21-23] and the presence of functional groups (such as hydroxyl and amine) makes them useful for conjugation. Rajaram et al. prepared Kaempferol (3, 5, 7, 4′ tetrahydroxy flavones) coated AuNPs, which shows the haemocompatible and anti-oxidant properties [24]. Moreover, the development of materials at the nano scale and their applications in different fields such as for biosensor and in biomedical and bioanalytical applications has been widely reported in the literature [25].

In particular, the chemical behaviour of AuNPs toward sensing of specific and selective metal ions can also open new avenues for trace level detection of various metal ions in various media specifically in aqueous media [26]. The detection of Al^{3+} has attracted the attention of the scientific community, due to the important role of Al^{3+} in causing disease states and its adverse effects on human health. Moreover, Al^{3+} toxicity endangers freshwater flora and fauna while the release of Al^{3+} from acidic soil has adverse effects on plant roots [27]. The entry of Al^{3+} into the human food chain occurs through water and acidic soil. Therefore, in the last few years the detection of Al^{3+} has drawn more attention. Recently, large number efflorescent probes have been developed for the detection of Al^{3+}. These probes work exceptionally well in organic

View Article Online
DOI: 10.1039/C6RA12076H

solvents, but have limited applications in aqueous media. The sensor's activities in non-aqueous media sometimes restrict their use in real-life applications, for example in environmental and biological samples. On the other hand, N-AuNPs have offered an easy alternative for the detection of metal ions in aqueous medium because of its high sensitivity and ease of operation.

Despite the vast applications of flavonoids, the structural details of the adsorption of these molecules on the AuNPs surface have not been studied in detail. To advance the understanding of the mechanisms driving the adsorption of flavonoids on the surface of AuNPs, we present a comprehensive study including the experimental and first-principles method based on DFT and TDDFT to determine the details of the interaction of naringin with the AuNPs.

Thus, in the present investigation, we report, bio inspired synthesis of AuNPs using naringin followed by surface engineering to construct nano theranostic agents. Naringin is used as reducing and stabilizing agents simultaneously. The N-AuNPs are completely characterized by means of various spectroscopic techniques using UV-Vis Spectroscopy, TEM, FT-IR, XRD and gel electrophoresis. The ability to integrate metal nanoparticles into biological systems has had great impact in biological applications. In this account, we discuss the plasmonic properties of naringin coated gold NPs and present examples of how they are being utilized for biodiagnostics, medical therapy and biosensing. The synthesized nanomaterials can be utilized in metastatic cancer cell biosensors. The malignant power (or stage of the tumour) is tested with the help of radiology imaging tests in which form of energy like x-rays or magnetic field is send through the body to take interior pictures. However, biosensor has potential to directly test the stage of the cancer. A combination of a biological and detector element of the biosensor allows for a small sample requirement, a compact design, rapid signals, rapid detection, high selectivity and high sensitivity for the analyte being studied. As compared to radiology imaging tests biosensors have the advantage of not only finding out how far the cancer has spread and checking if treatment is effective but also are cheaper and are more efficient to assess metastaticity in early stages of cancer.

Thus, N-AuNPs are used as biosensor to analyze Al^{3+} in aqueous media. In addition to this, these N-AuNPs are further subjected to hemolytic [28,29] and cytotoxicity assay [30,31] especially towards cancer cell lines to evaluate their feasibility in the transportation of drug in systemic circulation and their potential for other biological and therapeutic applications. From first-principles calculations, we have determined the (i) preferably interacting functional group of

View Article Online
DOI: 10.1039/C6RA12076H

the naringin, (ii) chemical bonding analysis of AuNPs and naringin, (iii) molecular orbitals of the naringin, which are responsible for the interaction with the AuNPs and (iv) theoretical analysis of the optical spectra upon binding of the naringin with the AuNPs.

Materials and Methods

Experimental All chemicals and reagents used in the present study are of analytical grade or of the highest purity available. Hydrogen tetrachloroaurate(III) trihydrate ($HAuCl_4.3H_2O$), Naringin, $Al(NO_3)_3.9H_2O$, $Cd(NO_3)_2.4H_2O$, $Fe(NO_3)_3.9H_2O$, $Sr(NO_3)_2$, $Mg(NO_3)_2.6H_2O$, $Co(NO_3)_2.6H_2O$, $Ni(NO_3)_2.6H_2O$, $Ca(NO_3)_2.4H_2O$, $Co(NO_3)_2.3H_2O$, $Ba(NO_3)_2$, $Zn(NO_3)_2.6H_2O$, $Hg(NO_3)_2].H_2O$ are purchased from Sigma Aldrich, India. All light and heavy metal salt solutions are prepared in triply distilled water. The glassware is washed with aqua regia (HCl: HNO_3=3:1(v/v)) and rinsed well with triply distilled water prior to use. The cell culture chemicals including Dulbecco's Modified Eagle's Medium (DMEM), L-15 medium, Ham-12 media, RPMI 1640 media, fetal bovine serum (FBS), penicillin-streptomycin antibiotic, phosphate buffered saline (PBS) and 0.25% (w/v) Trypsin, Trypan blue are purchased from Gibco, Invitrogen (Chandigarh, India). MTT [3-(4, 5-dimethyl-2-thiazolyl)-2, 5-diphenyltetrazolium bromide] is procured from HiMedia Laboratories (Mumbai, India).

Synthesis of Naringin conjugated gold nanoparticles

$HAuCl_4$ (0.4mM) and Naringin (0.05-0.5mM) are mixed in a buffer of pH = 9 in screw capped bottles. The components are mixed at room temperature. The bright yellow colour of solution disappears immediately to colourless solution. The solution is then placed at constant 40^{o}C with continuous stirring. The reduction process rate varies linearly with concentration of naringin. The solution with concentrations 0.05 mM, and 0.2 mM changed to respective coloured solutions within two hours of the reaction as shown in Figure SI-2a and 2b Supporting Information. Unlike the other solutions, [Naringin] = 0.5 mM (Figure 1a) changed to ruby red colour within two hours, indicating the formation of gold nanoparticles. Likewise, $HAuCl_4$ (0.2mM-1.2mM) and [Naringin] = 0.5 mM are mixed in a buffer of pH = 9 at room temperature. The resultant solution is then stirred at constant temperature of 40^{o}C. The colourless solution within two and half hour is changed to different colours, as shown in inset of Figure SI-2c, 2d, 2e Supporting Information. Further, temperature effect from 20^{o}C to 70^{o}C is studied on the synthesis of gold nanoparticles

View Article Online
DOI: 10.1039/C6RA12076H

from [HAuCl4] = 0.4 mM and [N] = 0.5 mM, which are found to be optimized concentrations as depicted from concentration effects. The samples for TEM, FT-IR, XRD and gel electrophoresis of optimized solution is prepared by centrifuging the solution at 10,000 rpm for 10 min and further two washings with triply distilled water at 10,000 rpm for 10 min are done to purify the sample.

Spectroscopic Analysis In order to understand the reaction kinetics of the synthesis of AuNPs, each reaction was monitored by simultaneous UV-Vis (on Hitachi Model No.U-3900, Double Beam) measurements. UV-Vis instrument is equipped with a TCC 240A thermoelectrically temperature controlled cell holder that allowed measurement of the spectrum at a constant temperature within ±1°C. The FT-IR spectra are recorded using a Perkin Elmer Spectrum 400 spectrometer with 1 cm^{-1} resolution with KBr pellets. The XRD studies of N-AuNPs are carried out with 'X'-Pert PRO, PANalytical. The samples are taken on a glass slide and the differactrogram are recorded using nickel-filtered CuKα radiation at a scanning rate of 0.6 deg 2(theta)/min.

pH Measurements An Accumet digital pH meter 910, fitted with a glass electrode is used for pH measurements of naringin and $HAuCl_4$ solution.

Microscopic probe N-AuNPs are characterized by TEM analysis on a JEOL2010F at an operating voltage of 200 kV. The samples are prepared by mounting a drop of a solution on a carbon coated Cu grid and allowed to dry in the air.

The Gel Electrophoresis The polarity of the N-AuNPs is determined by gel electrophoresis using TBE (tris-borate, 90 mM; ethylene diaminetetraacetic acid (EDTA), 2 mM, pH 8.0) buffer as a gel running medium. For this purpose, 1 % of aqueous agarose solution is first heated to boiling in a microwave, poured into a gel plate, and allowed to harden. Then 20 μL of an aqueous NP solution is loaded in each gel well, and a direct voltage of 90 V is applied for 10 min to promote the movement of NPs. No staining agent is needed because the N-AuNPs solution is colored.

Specific and selective metal ion detection assay The cation binding ability of N-AuNPs is evaluated from the changes in UV-Vis absorption spectra of N-AuNPs (10 μM) upon addition of

View Article Online
DOI: 10.1039/C6RA12076H

that metal salts (20 μM) in aqueous medium. The solutions are shaken for sufficient time before recording the spectra to ensure uniformity of solutions. For titrations, volumetric flask each containing standard solution of N-AuNPs (2.5 ml of 10 μM) along with varied amounts of $Al(NO_3)_3$ (0-20 μM) in aqueous solution is used.

Hemolytic Assay The hemolytic assay is performed to evaluate the response of N-AuNPs on blood group AB +ve of red blood cells (RBCs) from a healthy human donor. Briefly, a 5 % suspension of RBCs is used for this purpose after giving three washings along with two concentrations (i.e., 25 and 50 μg/mL) of each NP sample. One millilitre packed cell volume (i.e., hematocrit) is suspended in 20 mL of 0.01 M phosphate buffered saline (PBS). The positive control is RBCs in water, and it is prepared by spinning 4 mL of 5 % RBCs suspension in PBS. PBS as supernatant is discarded, and the pellet is resuspended in 4 mL of water. The negative control is PBS. All the readings are taken at 540 nm i.e. the absorption maximum of hemoglobin.

Ethical statements: In the present study, 4 ml of human blood is used in a controlled manner in our laboratory. All the experiments are performed for best practice according to the Panjab University guidelines. Further, consent of the donor has been taken before performing the experiment. We did not conduct any experimentation with animal subjects.

Cytotoxicity Assay

Cell Culture Different human cancer cell lines with variable genetic and hormonal background are used in the study. Human breast carcinoma cell lines MCF-7 (ER/PR +ve) , MDAMB-231 (ER/PR/HER-2 –ve), T47D (AR/ER/PR +ve) and human prostate carcinoma cell line PC-3 (AR -ve) are obtained from National Centre for Cell Sciences (NCCS), Pune, India. MCF-7, MDA MB-231, T47D and PC-3 are grown adherently and maintained in DMEM, L-15 medium, RPMI 1640 medium and Ham-12 medium, respectively, supplemented with 10 % FBS, 100 U/mL penicillin and 100 μg/mL streptomycin. MCF-7, T47D, PC-3 cells are incubated in a humidified atmosphere of 95 % air and 5 % CO_2 at 37°C while MDA MB-231 cells are maintained at 37°C in humidified CO_2 free atmosphere.

(ER- Estrogen Receptor, PR- Progesterone Receptor, AR-Androgen Receptor, HER- human epidermal growth factor receptor)

View Article Online
DOI: 10.1039/C6RA12076H

MTT cell proliferation assay

Effect of NPs treatment on the growth and viability of cancer cells (MCF-7, MDAMB-231, T47D and PC-3) is assessed by using the MTT assay in 3 replicates. Cells are seeded at concentration of 10×10^3 in serum supplemented media into 96-well culture plate and incubated overnight at 37ºC. After incubation for 24 hours to allow cell attachment, media is removed and replaced by serum less media for 24 hours, subjecting the cells to serum starvation. Thereafter, the cells are exposed to the different concentrations (30, 50 and 100 µg/ml) of N-AuNPs solution. After 24 hours of treatment, the media is removed and replaced with 100 µl of MTT (0.5 mg/ml) in media, and cells are incubated at 37ºC for 4 hours in dark. Supernatant is removed from the wells and the reduced MTT, formazan complex, is solubilized in 200 µl/well dimethyl sulfoxide (DMSO). Absorbance is measured at 570 nm using micro plate reader (Synergy H1, BioTek, USA).

Trypan blue exclusion assay

In another set of experiment, the rate of cell death with treatment is assessed by the trypan blue exclusion test. 2×10^5 cells are seeded in six well culture plates. After adhering to culture plates, cells are treated with different concentrations (30, 50 and 100 µg/ml) of N-AuNPs solution for 24 hours. After treatment, both floating cells in the medium and adhered cells on the plate are collected and concentrated by centrifugation. Cell viability is estimated after staining with 0.4 % trypan blue for 15 min. Both live (unstained) and dead (stained) cells are counted three times using countess automated cell counter (Invitrogen, India). The percentage of live cells and dead cells is used as an indicator for the viability of cells.

Cellular morphological analysis

For cytomorphological analysis, 2×10^5 cells are seeded in a 6-well culture plate and treated for 24 hours with N-AuNPs (100 µg/ml). Cells are photographed by confocal laser scanning microscope (Olympus FV-1200, Japan).

Computational Details

DFT is employed as a first principles quantum mechanical method. The method provides efficient and accurate estimates for the energies of molecules, binding energy and electronic

View Article Online
DOI: 10.1039/C6RA12076H

structure. The DFT calculations are performed using the 6-31G basis sets for C, H, O atoms and LANL2DZ double-split basis set for Au atoms with B3LYP functional (Becke's 3-parameter exchange functional with Lee–Yang–Parr correlation energy functional). The optimization is considered to be complete when energies and total forces drop below the respective thresholds of 1×10^{-4} Ry and 1×10^{-3} Ry a_0^{-1}. For optical response calculations, reminimisation of the naringin with Au_{13} cluster is performed with the long range corrected LC-ωPBE exchange correlation functional in the atomic orbital based NWCHEM package [32]. The functional is reasonably accurate because range corrected functional correctly reproduce long-range Coulomb decay. After reminimisation of the Au_{13} cluster with the functional groups of naringin, which is required to ensure the structures are local minima, the optical spectra of the complex are simulated from the Kohn-Sham state spectrum within the TDDFT framework, using configuration interaction singles. The analysis of the resulting spectra and the electronic composition of transitions is performed using the chemissian software package [33].

Results and Discussion

UV- Visible

The interaction of gold with naringin and its simultaneous use as reducing agent is studied in detail using UV-Vis spectroscopy by varying the concentration of naringin and $HAuCl_4$ salt with time at fixed 40°C and with temperature from 20°C to 70°C. Pure naringin (Supporting information, Figure SI-1b) at pH 9 and at 40°C shows two peaks at 336 nm (peak A) and 238 nm (peak B) corresponding to side chain A and B, respectively. The intensity of peak A and B increases with time. Such interesting UV-Spectra is characteristic of rich UV active molecules with –OH groups in conjugation with aromatic benzene rings, where these groups absorb UV light and transitions take place simultaneously with increased intensity [34]. Moreover at pH 9, phenolic -OH changes to phenoxide group, as a result conjugation increases and thus peak A is red shifted with increased intensity. However, there is no shift in absorption maxima of peak B because protons are stabilized by intramolecular H-bonding so phenoxide generation is not easy in side chain B. The shift in wavelength and intensity of peaks also indicate that the naringin released electrons, which can be used to cause reduction of Au(III) ions and to generate gold nanoparticle seeds[34].

View Article Online
DOI: 10.1039/C6RA12076H

Effect of initial concentration of naringin on rate of AuNPs formation

Upon addition of $HAuCl_4$, [$HAuCl_4$] = 0.4 mM to [N] = 0.05 mM, 0.1 mM, 0.2 mM and 0.5 mM, the absorption spectra is measured over a time interval of 120 minutes. On adding $HAuCl_4$ to [N] = 0.05 mM, N_1 (Figure SI-2a, Supporting Information), the intensity of peak A and peak B decreases. Similar results are observed at [N] = 0.1 mM, N_2 (not shown). The decrease in intensity of peaks A and B of naringin resulted because both phenoxide and condensed rings are directly involved in the reduction of Au (III) to Au (0) and thus indicates the formation of AuNPs with SPR band at 533nm, with less intensity and broader peak. At [N] = 0.2 mM, N_3 (Figure SI-2b, Supporting Information), peak A shows hyperchromic effect as well as bathochromic effect as in pure naringin, while intensity of peak B increases initially, then decreases and become constant with shift in peak from 283 to 287 nm. This red shift is directly associated with more electron donation from naringin to Au as a result SPR peak at 542 nm is blue shifted to 530 nm. For N_3, [N] = 0.2 mM, reaction mechanism clearly indicates that the variation in the intensity of all the peaks is inter related. The addition of $HAuCl_4$ will instantaneously direct $AuCl_4^-$ ions to the reducing site of side chain A and B to form ligands metal charge transfer (LMCT) complex. An increased intensity is related to the UV activity of naringin as well as formation of complex between ring A and ring B and $AuCl_4^-$ and instant fall in intensity indicates that reaction proceeds towards completion. However for N_4, [N] =0.5 mM (Figure 1a), reaction is fast and intensity of peak A and B increases, which might be attributed to the formation of N-AuNPs and UV active transitions of naringin itself. The variation in the intensities of peak B is more pronounced, which might be attributed to the strong interaction of condensed ring B of naringin with AuNPs with SPR peak shift from 540 nm to 525 nm over the time interval. This is further attributed to the formation of six-membered chelate ring between AuNPs and delocalised electron cloud of ring B, which is further, supported from first principle calculations.

To understand the role of naringin in the reduction of Au (III) to Au (0), a complete picture can be evaluated from wavelength vs time (Figure 1b) and intensity @ 525nm vs time (Figure 1c) plots at different concentrations of naringin. At lower concentrations (Figure 1b), N_1 and N_2, SPR peak decreases from 539 nm to 533 nm and from 538 nm to 534 nm, respectively. However, at high concentrations, N_3 and N_4, SPR decreases more from 542 nm to 530 nm and

View Article Online
DOI: 10.1039/C6RA12076H

540 nm to 525 nm. The decrease of λ_{max} with time is associated with the stabilizing properties of naringin molecule. Thus, at higher concentration of naringin, there is sufficient amount of naringin to stabilize AuNPs. Figure 1c reveals the change in intensity @ 525 nm vs time plots. Both the plots of wavelength and intensity vs time support each other. As wavelength decreases, intensity of the corresponding concentrations of naringin increases, which is again associated with the stability of AuNPs. A variation in these peaks explains the reaction mechanism on how reduction is initiated to generate nucleating centres, which eventually convert into NPs. As reduction initiates, it consumes $AuCl_4^-$ ions through LMCT complex and produces AuNPs. The character of the obtained kinetic curve in Figure 1c is sigmoidal and it is typical of the precious metals nanoparticles formation [35]. These sigmoidal kinetic curves describe two stage process of nanoparticle synthesis responsible for slow nucleation and fast autocatalytic growth during the progress of the reaction in each case. It confirms that process of nucleation is slow and growth is catalytic. All the plots show that naringin starts nucleation within ≈ 5 minutes at all concentration although the magnitude is much higher for N_4 instead of lower concentrations. The greater magnitude of curve (i.e. plateau region) for N_4 is basically related to stable and the greater number density of NPs produced. Thus, reduction is most facilitated at [N] = 0.5 mM and least at [N] = 0.05 mM. It is expected that with increasing concentration of naringin, the process of nanoparticles formation runs faster, because more nuclei are created at the same time. Using registered kinetic curves, observed rate constant for growth processes are derived. First order rate constant values (provided by choosing maximum points) for N_1, N_2, N_3 and N_4 are 2.46×10^{-4} s^{-1}, 2.55×10^{-4} s^{-1}, 4.26×10^{-4} s^{-1} and 6.5×10^{-4} s^{-1} respectively.

Effect of gold salt precursor concentration on the rate of nanoparticles formation

The influence of different concentration of $HAuCl_4$ ([$HAuCl_4$] = 0.2 mM (Au_1), 0.4 mM (Au_2), 0.6 mM (Au_3) and 1.2 mM (Au_4)) by selecting suitable concentration of naringin i.e. N4 (as described in the previous reaction) where [N] = 0.5 mM is also studied. In all the plots, there is no significant change in the wavelength of peak A and peak B on addition of Au salt (changes are comparable to blank naringin at pH 9, Figure SI-1b, Supporting Information). However, intensity of peak A and peak B initially increases and later become constant, which reveals the formation of LMCT between $AuCl_4^-$ and naringin and completion of the reaction, respectively.

View Article Online
DOI: 10.1039/C6RA12076H

Plots of maximum wavelength vs time for Au_1, Au_2, and Au_3 reveals that wavelength decreases from 537 nm to 518 nm, 544 nm to 525 nm and 541 nm to 540 nm (Figure 1d). However, for Au_4, SPR shifts from 547 nm to 584 nm. To further understand this behaviour, intensity @ 525 nm vs time is plotted which shows (Figure 1e) that the intensity increases with increase in the concentration from 0.2 mM to 0.4 mM and decreases from 0.6 mm to 1.2 mM. Thus, naringin is not sufficient to stabilize AuNPs at higher concentrations of gold salt. However, at lower concentrations of gold salt, naringin act as reducing and stabilizing agent.

In each experiment, kinetic curves related to nucleation, growth and stability of AuNPs is registered. The kinetic curve is sigmoidal in each case. Rate of nucleation seems to be same at all concentrations of $[HAuCl_4]$. However, rate of growth decreases with increase in concentration of $[HAuCl_4]$ because naringin is not sufficient to cause complete reduction and stability. The rate constant values for Au_1, Au_2, Au_3, and Au_4 are 5.66×10^{-4} s^{-1}, 8.93×10^{-4} s^{-1}, 3.46×10^{-4} s^{-1} and 3.26×10^{-4} s^{-1} respectively, which also decrease with increase in concentration of $[HAuCl_4]$.

Thus, it can be concluded that equimolar quantities of gold and naringin are most suitable for producing stable AuNPs.

Temperature Effect

Figure 1f shows the change in absorbance versus wavelength over a temperature range from 20°C to 70°C. It reveals that reduction does not take place at 20°C and 30°C. It starts at 40°C and the solution changes colour from yellow to ruby red within 2 hours while at 50, 60 and 70°C, the solution remains mustard brown which indicates incomplete reduction and stabilization of gold salt by naringin. To comprehend, the time effect is studied at individual temperature (i.e. 40, 50, 60 and 70 °C) (Figure SI-3, Supporting information). 40°C is the optimized and appropriate temperature for the nucleation and growth of gold nanoparticles, thus resulted into the formation of electrostatically stable gold sol. The predicted mechanism can be explained on the basis of formation of LMCT. The extent of LMCT is maximum at 40°C and then starts decreasing with increasing temperature beyond 40°C. This is attributed to the chemical desorption of the adsorbate, naringin from the AuNPs surface and degradation of flavonoids at high temperatures [36].

View Article Online
DOI: 10.1039/C6RA12076H

TEM It has been shown that SPR band position and intensity are mainly determined by the morphology of the particles [37]. Here, sharp and narrow SPR peak at 525 nm imply that reaction between [HAuCl4] = 0.4 mM and [N] = 0.5 mM has generated spherical AuNPs and is supported from TEM. TEM system is used to characterize the morphology and size of N-AuNPs (Figure 2a). The spherical particles with average size 23 nm are observed and corresponding histogram of particle size distribution of N-AuNPs is shown in Figure 2b. Most of the particles are in the size range of 20-25 nm. Thus, better control of the particle size and monodispersity are achievable through the use of naringin.

FTIR and XRD The synthesis of AuNPs by naringin is further supported from FT-IR studies (Supporting information, Figure SI-4). Bands at 1581 cm^{-1}, 1520 cm^{-1} and 1450 cm^{-1} in N due to aromatic C=C stretching merge into 1540 cm^{-1} in N-AuNPs, which suggest presence of naringin in AuNPs. Further, mergence of all C=C stretching into one band shows involvement of all π- of aromatic rings in AuNPs formation. Bands due to phenolic C-OH stretching at 1365 cm^{-1} shift to 1378 cm^{-1} and at 1294 cm^{-1} and 1203 cm^{-1} merge to 1224 cm^{-1} in N-AuNPs, which suggest the participation of phenolic –OH groups in forming AuNPs. Further, bands due to glucose C-OH stretching at 1147 cm^{-1}, 1140 cm^{-1}, 1092 cm^{-1}, 1065 cm^{-1}, 1038 cm^{-1} merge into bands at 1163 cm^{-1} and 1050 cm^{-1}, indicate the presence of glucose moiety in N-AuNPs. Band at 1646 cm^{-1} due to C=O stretching shifts to 1636 cm^{-1}, indicating its involvement in AuNPs formation. The band at 3427 cm^{-1} due to -OH stretching shows a hypsochromic shift to 3389 cm^{-1} which indicates the weakening of bond strength of -OH group of glucose moiety due to its solvation at pH 9. The solvation effect is further supported by gel electrophoresis (Supporting information, Figure SI-5) which reveals the presence of negative charge on N-AuNPs surface. These interactions are further supported from first principles calculations discussed later in this section.

The crystal structure and phase composition of N-AuNPs are further characterized by XRD. XRD patterns are shown in Supporting information, Figure SI-6 and all diffraction peaks can be indexed to Au face centered cubic geometry with predominant growth at (111) crystal planes. The peaks at 2Φ=38.3, 44.6, 64.7, 77.5 are indexed as (111), (200), (220) and (311) planes for AuNPs. The results agree well with reported standards (JCPDS file no. 04-0784).

Gel Electrophoresis The polarity of N-AuNPs can be evaluated by gel electrophoresis and the results are presented in Supporting information, Figure SI-5. The sample move towards the

View Article Online
DOI: 10.1039/C6RA12076H

positive terminal of the battery, which is expected due to negatively charged AuNPs surface because of the solvation of -OH groups of naringin coated on the surface of AuNPs. This shows that naringin acts a fine stabilizing agent apart from its reducing behaviour.

First Principles Calculations

We have selected a gold cluster of 13 atoms and optimized its geometry. The flavonoids can interact with the AuNPs through the side chains marked A and B in Supporting information Figure SI-1a. In order to study the relative difference in interactions of these groups with the AuNPs, we have selected the two functional groups $[C_6H_5O]^-$ and $[C_{10}H_7O_2]$ of naringin which are representative structures of the two side chains A and B of the naringin, respectively. These functional groups are optimized independently. Then the optimized structures of these groups were placed individually at a distance of around 2.0 Å from the Au_{13} cluster. During the geometry optimization, all the atoms are allowed to relax in x-, y- and z-directions. The Binding energy (BE) is calculated by

$$BE = [E_{Func.\ A/B\ and\ Au13} - (E_{Func.\ A/B} + E_{Au13})]$$

where $E_{Func.\ A/B\ and\ Au13}$ is the total energy of the relaxed functional A/B-Au_{13} system, $E_{Func.\ A/B}$ is the energy of the functional group A/B and E_{Au13} is the energy of the Au_{13} cluster. The stable structures will have negative BE values. The optimized structure of $[C_{10}H_7O_2]$ and $[C_6H_5O]^-$ on the Au_{13} cluster is shown in the Supporting information, Figure SI-7a, 7b respectively. The calculated BE values for the $[C_6H_5O]^-$-Au_{13} and $[C_{10}H_7O_2]$-Au_{13} systems are presented in table 1. The most stable structure of $[C_6H_5O]^-$ on Au_{13} had a BE of 1.88 eV, while the most stable structure of $[C_{10}H_7O_2]$ had a BE of 2.15 eV. The magnitude of the BE of the two functional group indicates that the interaction is strong, however the functional group $[C_{10}H_7O_2]$ interacts more strongly in comparison to the $[C_6H_5O]^-$. The Lowdin charge analysis (Table 1) of the $[C_6H_5O]^-$-Au_{13} and $[C_{10}H_7O_2]$-Au_{13} systems reveals a charge transfer during the interaction. However, the charge transfer is comparatively higher in the case of $[C_{10}H_7O_2]$-Au_{13} (.21), which then leads to the higher BE values. The simulation results, basically originate from donation of the electrons from naringin to the Au atoms. The electron cloud is more delocalized in the functional group $[C_{10}H_7O_2]$ than in $[C_6H_5O]^-$. The present results provide evidence verifying the role of the functional group $[C_{10}H_7O_2]$ in auric chloride reduction more strongly than $[C_6H_5O]^-$.

View Article Online
DOI: 10.1039/C6RA12076H

Figure 3(a) and 3(b) shows the highest occupied molecular orbital (HOMO) and lowest unoccupied molecular orbital (LUMO) of the $[C_{10}H_7O_2]$-Au_{13} system. The orbitals associated with functional groups appear as HOMO in the two complexes studied, whereas the LUMO is associated with the Au atoms. However, there is a difference in the HOMO of the two functional groups i.e. HOMO in case of $[C_{10}H_7O_2]$ is more delocalized than $[C_6H_5O]^-$. The vertical excitation spectrum of the system is studied theoretically with TDDFT. The theoretical spectra of the $[C_6H_5O]^-$-Au_{13} and $[C_{10}H_7O_2]$ -Au_{13} are displayed in the Figure 4(a) and 4(b) with a Gaussian convolution of 0.2 eV, in order to represent experimental broadening. The complex $[C_6H_5O]^-$-Au_{13} shows the major excitations centred on 2.526 eV (490 nm), which contain significant oscillator strength. The $[C_{10}H_7O_2]$-Au_{13} shows the major excitations around 2.983 eV (415 nm). The peak in the Vis region has shifted down for the $[C_{10}H_7O_2]$-Au_{13} conjugate system in the wavelength resulting in a more stable complex than $[C_6H_5O]^-$-Au_{13}. Table 2 and 3 shows the MO pairs which provide greater than 5% of the intensity for $[C_{10}H_7O_2]$-Au_{13} and $[C_6H_5O]^-$-Au_{13} respectively. It is found that the first and second largest contributions are same for both the cases and it is due to d to s transition in Au cluster. However for the $[C_{10}H_7O_2]$-Au_{13} third most prominent transition is from the MO 158 to 166 which is from the delocalized p electrons of $[C_{10}H_7O_2]$ to s states of Au. This transition is absent in case of $[C_6H_5O]^-$-Au_{13} and it is responsible for shifting of the peak towards shorter wavelength. The particle-hole pairs of NTOs for the vertical excitation in $[C_{10}H_7O_2]$-Au_{13} and $[C_6H_5O]^-$-Au_{13} are shown in the Figure 5 and Figure SI-8, Supporting Information respectively. The hole state of the excitation is localized on the functional group $[C_{10}H_7O_2]$ of the naringin and the particle state is localized on the Au cluster. Thus, the NTO analysis provides evidence for the nature of interaction as provided by the electronic structure calculations. The hole and particle states are increasingly localized on $[C_{10}H_7O_2]$ and Au_{13} respectively for the higher energy transitions in addition to the low energy transitions, whereas in case of $[C_6H_5O]^-$-Au_{13} system they are localized only for the low energy transitions and for higher energy transitions both hole and particle states are increasingly localized on Au_{13} (Figure SI-8, Supporting Information).

We have tested the interactions of the two functional groups of the naringin on a larger cluster of Au atoms. For this purpose we have optimized a cluster of 32 atoms of the Au. This cluster is also optimized with the same basis set and functional previously we have used for the cluster of 13 atoms. The bond lengths obtained in our simulation for this cluster are in agreement

View Article Online
DOI: 10.1039/C6RA12076H

with the values obtained previously in the literature [38]. We have studied the interactions of the $[C_{10}H_7O_2]$ and $[C_6H_5O]^-$ with the Au_{32} cluster. In this optimization also we have found that the functional $[C_{10}H_7O_2]$ had higher BE in comparison to that of $[C_6H_5O]^-$. Figure SI-9a, 9b Supporting Information shows the optimized configuration of $[C_{10}H_7O_2]$ and $[C_6H_5O]^-$ on Au_{32} cluster, respectively. Although the relative value of the BE in case of Au_{32} has decreased but the order remains the same. This has happened due to the high stability and exceptional properties of the newly found magic number 32 due to the relativistic effects, high HOMO-LUMO energy gap, and aromaticity of the Au_{32} cage [39, 40]. TDDFT analysis of $[C_{10}H_7O_2]/Au_{32}$ has major excitations centred at 2.14 eV (578 nm) whereas $[C_6H_5O]^-$-Au_{32} has peak at 2.06 eV (601 nm). There is shift in peak in the visible region at lower wavelengths of $[C_{10}H_7O_2]$-Au_{32} conjugate system in comparison to that of $[C_6H_5O]^-$-Au_{32} complex, confirming the results previously obtained with the smaller cluster.

Metal Ion Recognition Ability of N-AuNPs

The N-AuNPs in the present study is tested for their application as a calorimetric sensor for detection of metal ions. The metal ion detection ability of N-AuNPs is studied separately for each of the metal ions involving Al(III) Fe(III), Cr(III), Ba(II), Hg(II), Sr(II), Cd(II), Co(II), Mg(II), Mn(II) and Ag(I) at a fixed concentration of 20 μM. The change in the absorbance of N-AuNPs in the presence of metal ions is monitored using UV-Vis Spectroscopy as shown in Figure SI-10a, Supporting Information. Upon addition of Al^{3+} (20 μM) to N-AuNPs solution (10 μM), the color of the solution changes immediately from red to blue (Figure SI-10a Supporting Information inset) within two minutes having a remarkable change in intensity and wavelength of SPR peak. There is bathochromic shift from 525 nm to 545 nm and hypochromic effect from 1.03 to 0.78. This method allows the naked eye to detect Al^{3+} with high selectivity over other metal ions. The other ions investigated here show a slight change in the intensity and SPR peak wavelength implying that most of these metal ions cannot undergo any complexation with N-AuNPs. Thus, it demonstrates the high selectivity and sensitivity of N-AuNPs towards Al^{3+}. The changes in absorption intensity, ΔA and wavelength, $\Delta\lambda$ after the addition of different metal ions to N-AuNPs are shown in Figure SI-10b-10c, Supporting Information.

Similarly quantitative Al^{3+} array for direct calorimetric visualization is done by adding various concentrations (0-20 μM) of Al^{3+} to N-AuNPs solution. It is done to find the minimum

View Article Online
DOI: 10.1039/C6RA12076H

concentration to probe the selective and specific metal ion detection. As shown in Figure SI- 11a, Supporting Information with increasing concentration of Al^{3+}, there is a gradual bathochromic shift observed in SPR band of AuNPs, indicating the aggregation of particles, and the colour of the solution changed from red to blue. The changes in intensity and SPR band are noted using UV-Vis spectroscopy, which is further supported from TEM analysis (Figure 2c). TEM shows that the average size of the N-AuNPs increases in the presence of Al^{3+} from 23 nm to 35 nm (Figure 2c). The absorbance ratio (A_{640}/A_{520}) (Figure SI-11b, Supporting Information) is found to vary almost linearly with an increase in the concentration of Al^{3+} from 2 to 20 μM, and the values of linear regression coefficient (R^2) is found to be 0.99987 with a detection limit of 0.1 mg/ml. This detection limit is significant because its value is in the range of secondary maximum contaminant level (SMCL) for Al in drinking water defined by WHO/FAO [41, 42].

We also investigated the real water samples i.e. our lab tap water. There was no colour change on adding the N-AuNPs to the water, which might be due to low concentration of Al^{3+} in tap water samples. Thus, different concentrations of Al^{3+} ions are spiked to tap water samples and the ability of N-AuNPs to detect these metal ions is analyzed. The colour change of tap water samples is shown in Figure 6a. A linear decrease in the absorption intensity of AuNPs at 525nm was observed at a concentration of Al^{3+} ranging between 0.01μM and 100μM (Figure 6b). The lowest detectable concentration of Al^{3+} in tap water was estimated to be 0.1mg/ml. The absorption ratio (A_{640}/A_{520}) of N-AuNPs showed a linear increase in Al^{3+} concentration in tap water ranging between 0.05μM and 100μM (Figure 6c). The metal ion detection ability of AuNPs was significantly different when tested with tap water in comparison to that of distilled water. This may be due to the presence of some impurities in drinking water and tap water that could influence the detection ability of metal NPs.

Mechanism for nanoparticle aggregation

On the basis of present study we propose a possible mechanism of interaction of N-AuNPs with metal ions, Al^{3+}, which is shown in Scheme 1. This interaction leads to bathochromic shift in the SPR band with an increase in the concentration of Al^{3+} ions from 0-20 μM. According to the hard and soft acid and base (HSAB) principle, -OH is a hard base which can strongly coordinate with Al^{3+}, a hard acid. Thus, the complexing action of –OH of neohesperidose, a disaccharide functionality of the naringin on the surface of AuNPs and Al^{3+}, leads to the aggregation of NPs.

View Article Online
DOI: 10.1039/C6RA12076H

Further, Al^{3+} has very high charge density and small ionic radius [43], thus interacts strongly as compared to other metal ions.

Biological Applicability

Hemolysis In addition to the use of naringin as food supplement, inhibitor of VEGF release and drug, it's coated AuNPs show remarkable biological applicability, which is demonstrated by performing hemolytic assays. Hemolysis is a process in which foreign substances can interact and rupture the RBCs cell membrane and release hemoglobin [28]. A similar mechanism is expected if NPs interact with RBCs in the bloodstream when they are planned for use in various biological applications that might require their intravenously administrated formulations. Uncoated AuNPs surface has a high surface energy to interact with the cell wall of a blood cell, which causes deformation and eventually hemolysis [30, 44]. Moreover, hemolysis depends on the morphology and size of NPs, naked NPs have far more potential to interact with blood cell and thus demonstrate pronounced hemolytic effect. In fact, the cell membrane consists of three layers with glycocalyx on the exterior, a protein network on the interior, and a lipid bilayer in between the two. Glycoprotein layer is highly susceptible to complexation due to the predominant hydrophilic interactions with bare Au NP surface and hence, they are responsible for the rupturing of the blood cell. However, when the bio inspired substances such as naringin is coated on the AuNPs surface, the hemolytic response is markedly reduced. Furthermore, naringin is a bulky molecule and hence uniformly cover the Au NPs surface and hence reduce the risk of hemolysis to the maximum extent. Thus, N-AuNPs with concentrations 25 µg/ml and 50 µg/ml are subjected to hemolysis to identify minimum concentration that provides minimum hemolysis and hence is best suited for the drug delivery vehicles in the systematic circulation. Typical examples of two samples with part of heme absorption spectrum within 500 to 600 nm of wavelength range are illustrated in Figure SI- 12a, Supporting Information (enlarged view in Figure SI-12b Supporting Information) for 25 µg/ml and 50 µg/ml, respectively with positive and the negative controls (see Experimental Methods section), along with different dose concentrations of Au NPs. Table 4 reveals that the values of percentage hemolysis [(sample absorbance − negative control absorbance)/(positive control absorbance − negative control absorbance) × 100] for N-AuNPs at two dose concentration of 25 µg/ml and 50 µg/ml are 0.74 and 1.2, respectively. The hemolysis increases with the increase in the amount of NPs for both

View Article Online
DOI: 10.1039/C6RA12076H

mixtures because greater number of NPs have great potential to break the cell wall, hence it is minimum for 25 µg/ml and decreases with decrease in concentration of N-AuNPs, which can be used as drug release vehicle in the systemic circulation.

Cytotoxicity

Effect of NPs on cell viability

Figure 7(a-d) shows the plot of MTT Absorbance with increasing concentrations of N-AuNPs in the range of 30–100 µg/ml. MTT Absorbance is directly related to the cell viability. Thus, N-AuNPs shows cytotoxic effect on MCF-7, T47D and PC-3 cells (Figure 7a-c), however in contrast these exhibit significant proliferative effects on estrogen-independent MDAMB-231 (Figure 7d) breast cancer cells. Data shows a significant decline in cells viability in MCF-7 (78.8%, 50.6% and 48.9% at 30, 50 and 100 µg/ml concentrations of N-AuNPs, respectively), T47D (79.1%, 70.2% and 58.9% at 30, 50 and 100 µg/ml concentrations of N-AuNPs, respectively) and PC-3 (71.8%, 63.9% and 54.8% at 30, 50 and 100 µg/ml concentrations of N-AuNPs, respectively). Enhanced proliferative activity is observed in MDAMB-231 cells as NPs treatment exerts increase in cell viability (132.7% at 50 µg/ml concentrations of N-AuNPs)

Also cell viability in response to NPs is evaluated by trypan blue exclusion test for which cells are exposed to NPs for 24 hours (Figure 8a-d). After incubation with NPs, cells exhibit reduction in viability up to 33% in MCF-7, 34% in T47D and 33% in PC-3 cells at 100 µg/ml concentration of N-AuNPs (Figure 8a-c). In contrast, MDAMB-231 (Figure 8d) cells shows increase in cell viability by 119% on treatment with 50 µg/ml concentration of N-AuNPs. Further these experiments have shown that there is direct dose–effect relationship for the cytotoxicity between the content of Naringin on the Au NPs surface and cancer cell line. The content of Naringin in Naringin-AuNPs complex produces significant cytotoxicity to cells in dose-dependent manner in the concentration range of 30-100 µg/mL.

Cytotoxic effects of flavonoids on breast and prostate cancer cells are highly related to the expression of hormone receptors. Breast and prostate cancers are hormone-dependent tumors as their development and growth can be dependent on the expression of estrogen receptors (ER) and androgen receptors (AR), respectively. Both breast carcinoma cell lines MCF-7 (ER/PR +ve) & T47D (ER/PR/AR +ve) and androgen-independent prostate cancer cell line PC-3 (ER +ve /AR

View Article Online
DOI: 10.1039/C6RA12076H

-ve) are hormone sensitive cell lines especially expressing estrogen receptors. Studies [45] have revealed that naringin shows double directional adjusting function of estrogenic and anti-estrogenic activities i.e. promoted cytotoxicity in cancer cells by acting in dual manner-estrogenic agonist agent as well as an estrogenic antagonist. Naringin produce estrogenic and anti-estrogenic effects primarily through selectively binding with estrogen receptor β. The Naringin-AuNPs will quench/block the estrogen receptor pathway signaling leading to stoppage of cell proliferation i.e. inducing cytotoxicity. This has been confirmed by similar type of experiments performed on triple negative breast cancer cell line MDA MB 231 (ER/PR/HER-2 – ve) which instead of cytotoxicity shows proliferation at all the concentrations of Naringin-AuNPs. Since the cells lack hormonal receptors thereby Naringin-AuNPs gets ineffective to induce any impact which they exhibit in cells with hormonal receptor.

Cytomorphological Analysis

The cytomorphological examinations (Figure SI-13, Supporting Information) of cancer cells (MCF-7, T47D and MDAMB-231) are observed and photographed using confocal laser scanning microscope (Olympus FV-1200, Japan). The analysis shows that cells are in their typical epithelial morphology in untreated controls of MCF-7, T47D, and MDAMB-231 (Figure SI-13a, 13c and 13e, Supporting information). However, adverse effects are manifested in MCF-7 and T47D cells when exposed to 100 µg/ml of N-AuNPs result into deterioration of cellular morphology (Figure SI-13b and 13d, Supporting information). Also, treatment reduces the density of cells in comparison to untreated controls as evident. However, MDAMB-231 (Figure SI-13f, Supporting information) cells do not show any significant change in its morphology and cell number.

Conclusions

In conclusion, the present study reports a simple, economical and environmentally friendly approach for the synthesis of AuNPs using naringin-a flavonoid, in aqueous medium. N-AuNPs are characterized by UV-Visible, TEM, FT-IR, and XRD techniques. Naringin acted as both reducing and capping agent for AuNPs under mild conditions. First-principles calculations based on DFT are performed to study the interaction of naringin on AuNPs. We find that both the functional

View Article Online
DOI: 10.1039/C6RA12076H

groups $[C_6H_5O]^-$ and $[C_{10}H_7O_2]$ interact strongly with the Au_{13} cluster, however the group $[C_{10}H_7O_2]$ has largest BE energy, mediated by the higher charge transfer to the AuNPs. The present study does support the experimental finding of a Naringin-Au complex formation. Molecular orbital analysis suggests that the orbitals produced by coupling of AuNPs with $[C_{10}H_7O_2]$ are more delocalized than the orbitals of $[C_6H_5O]^-$. TDDFT analysis confirms that the major peak in the absorption spectra of $[C_{10}H_7O_2]$-Au_{13} shifts to lower wavelength resulting in a more stable system. TDDFT calculations predict that hole state of the excitation are localized on the naringin and particle states on Au atoms of $[C_{10}H_7O_2]$-Au_{13} complex. The synthesized N-AuNPs are used as calorimetric sensor for the detection of Al^{3+} ion. This calorimetric sensor could be used in both quantitative and qualitative detection of Al^{3+}, with the detection limit of 0.1 mg/ml. The color change from red to blue is easily visualized with naked eye. This simple, rapid and cost-effective sensing system appears to be holding great practicality for detection of Al^{3+} in real samples. Further N-AuNPs are assessed with hemolysis and cytotoxicity assays, which suggest their biocompatibility with normal red blood cells and MDAMB-231 cell lines, while showing the potential to cause cell death in MCF-7, T47D and PC-3. Thus, N-AuNPs opens up several possibilities for its use in various biomedical applications, which require their intravenous administration as well as in sensing properties. This work also serves as the first-step toward gaining the understanding of interactions of flavonoids with AuNPs by using first principles methods.

Acknowledgments

The authors acknowledge the Council of Scientific and Industrial Research (CSIR), New Delhi, India for their financial support (Project No: 01(2700)/12/EMR-II).

References

1. J.B. Harborne and C.A. Williams, Advances in flavonoid research since 1992, *Phytochemistry,* **2000**, 55, 481-504.

View Article Online
DOI: 10.1039/C6RA12076H

2. R.J. Nijveldt, E. van Nood, D.E. van Hoorn, P.G. Boelens, K. van Norren and P.A. van Leeuwen, M. Flavonoids: a review of probable mechanisms of action and potential applications, *Am. J. Clin. Nutr.,* **2001**, 74, 418-425.
3. L. de Lira Teixeira, F.C. Bertoldi, F.M. Lajolo and N.M.A. Hassimotto, Identification of Ellagitannins and Flavonoids from Eugenia brasilienses Lam. (Grumixama) by HPLC-ESI-MS/MS, *J. Agric. Food Chem.*, **2015**, 63, 5417–5427.
4. M. Sökmen, J. Serkedjieva, D. Daferera, M. Gulluce, M. Polissiou, B. Tepe, H.A. Akpulat, F. Sahin and A. Sokmen, In Vitro Antioxidant, Antimicrobial and Antiviral Activities of the Essential Oil and Various Extracts from Herbal Parts and Callus Cultures of Origanum acutidens, *J. Agric, Food Chem*., **2004**, 52, 3309-3312.
5. T. Fang, Y. Wang, Y. Ma, W. Su, Y. Bai and P Zhao, A rapid LC/MS/MS quantitation assay for naringin and its two metabolites in rats plasma, *J Pharmaceut Biomed,* **2006**, 40, 454-459.
6. T. J. Mabry, Selected Topics from Forty Years of Natural Products Research: Betalains to Flavonoids, Antiviral Proteins, and Neurotoxic Nonprotein Amino Acids, *J. Nat. Prod.*, **2001**, 64, 1596–1604.
7. E. Genoux, E. Nicolle and A. Boumendjel, Flavonoids as Anticancer Agents: Recent Progress and State of the Art?, *Curr. Org. Chem.,* **2011**, 15, 2608-2615.
8. L.A. Savi, T. Caon, A.P. de Oliveira, A.M. Sobottka, W. Werner, F.H. Reginatto, E.P. Schenkel, C.R.M. Barardi and C.M.O. Simoes, Evaluation of antirotavirus activity of Flavonoids, *Fitoterapia*, **2010**, 81, 1142-1146.
9. T. Tanaka and R Takahashi, Flavonoids and Asthma, *Nutrients,* **2013**, 5, 2128-2143.
10. B.H. Havsteen, The biochemistry and medical significance of the Flavonoids, *Pharmacol Ther,* **2002**, 96, 67-202.
11. T. Annadurai, P.A. Thomas and P. Geraldine, Ameliorative effect of naringenin on hyperglycemia-mediated inflammation in hepatic and pancreatic tissues of Wistar rats with streptozotocin- nicotinamide-induced experimental diabetes mellitus, *Free Radic Res*., **2013**, 47, 793-803.
12. Y. Chen, R. Zheng, J. Zhongjian and J. Yong, Flavonoids as superoxide scavengers and antioxidants, *Free Radic. Biol. Med.,* **1990,** 9, 19-21.

View Article Online
DOI: 10.1039/C6RA12076H

13. F.V. So, N. Guthrie, A.F. Chambers, M. Moussa and K.K. Carroll, Inhibition of human breast cancer cell proliferation and delay of mammary tumorigenesis by flavonoids and citrus juices, *Nutr. Cancer,* **1996**, 26, 167-181.
14. R.G. Tilton, T. Kawamura, K.C. Chang, Y. Ido, R.J. Bjercke, C.C. Stephan, T.A. Brock and J.R. Williamson, Vascular dysfunction induced by elevated glucose levels in rats is mediated by vascular endothelial growth factor, *J Clin Invest*., **1997**, 99, 2192-2202.
15. A. Kumar, S. Dogra and A. Prakash, Protective Effect of Naringin, a Citrus Flavonoid, Against Colchicine-Induced Cognitive Dysfunction and Oxidative Damage in Rats, *Journal of Medicinal Food,* **2010**, 13, 976-984.
16. H. Lotz-Winter, On the pharmacology of bromelain: an update with special regard to animal studies on dose-dependent effects, *Planta Med,* **1990**, 56, 249-253.
17. N. Lin, J. Huang and A. Dufresne, Preparation, properties and applications of polysaccharide nanocrystals in advanced functional nanomaterials: a review, *Nanoscale*, **2012**, 4, 3274.
18. P. Raveendran, J. Fu and S.L. Wallen, Completely "green" synthesis and stabilization of metal nanoparticles, *J. Am. Chem. Soc*., **2003**, 125, 13940−13941.
19. K.B. Narayanan and N. Sakthivel, Biological synthesis of metal nanoparticles by microbes, *Adv. Colloid Interface Sci.,* **2010**, 156, 1−13.
20. A.K. Mittal, J. Bhaumik, S. Kumar and U.C. Banerjee, Biosynthesis of silver nanoparticles: elucidation of prospective mechanism and therapeutic potential, *J. Colloid Interface Sci.*, **2014**, 415, 39−47.
21. J.R. McCarthy, J. Bhaumik, M.R. Karver, S.S. Erdem and R.W. Weissleder, Targeted nanoagents for the detection of cancers, *Mol. Oncol*, **2010**, 4, 511−528.
22. F.M. Kievit and M. Zhang, Cancer nanotheranostics:improving imaging and therapy by targeted delivery across biological barriers, *Adv. Mater*. **2011**, 23, H217−H247.
23. Y. Gong and F.M. Winnik, Strategies in biomimetic surface engineering of nanoparticles for biomedical applications, *Nanoscale*, **2012**, 4, 360−368.
24. B.S. Raghavan, S. Kondath, R. Anantanarayanan and R. Rajaram, Kaempferol mediated synthesis of gold nanoparticles and their cytotoxic effects on MCF-7 cancer cell line, *Process Biochemistry,* **2015**, 50, 1966-1976.

View Article Online
DOI: 10.1039/C6RA12076H

25. L. Prodi, Luminescent chemosensors: from molecules to nanoparticles, *New J. Chem.,* **2005**, 29, 20-31.
26. A. Singh, S. Kaur, N. Singh, N. Kaur, Fluorometric sensing of Hg^{2+} ions in aqueous medium by nano-aggregates of a tripodal receptor, *Org. Biomol. Chem*., **2014**, 12, 2302-2309.
27. O. Deschaume, A. Fournier, K.L. Shafran and C.C. Perry, Interactions of aluminium hydrolytic species with biomolecules, *New J. Chem.,* **2008**, 32, 1346-1353.
28. A. Mahal, P. Khullar, H. Kumar, G. Kaur, N Singh, M.J. Niaraki and M.S. Bakshi, Green Chemistry of Zein Protein Toward the Synthesis of Bioconjugated Nanoparticles: Understanding Unfolding, Fusogenic Behavior, and Hemolysis, *.ACS Sustainable Chem. Eng.,* **2013**, 1, 627-639.
29. M.K. Goshisht, L. Moudgil, P. Khullar, G. Singh, A. Kaura, H. Kumar, G. Kaur and M.S. Bakshi, Surface Adsorption and Molecular Modeling of Biofunctional Gold nanoparticles for Systematic Circulation and Biological Sustainability, *ACS Sustainable Chemistry & Engineering,* **2015**, 3, 3175-3187.
30. M.A. Dobrovolskaia, J.D. Clogston, B.W. Neun, J.B. Hall, A.K. Patri and Scott E. McNeil, Method for Analysis of Nanoparticle Hemolytic Properties in Vitro, *Nano Lett.*, **2008**, 8, 2180-2187.
31. M.K. Goshisht, L. Moudgil, M. Rani, P. Khullar, G. Singh, H. Kumar, N. Singh, G. Kaur and M.S. Bakshi, Lysozyme Complexes for the Synthesis of Functionalized Biomaterials To Understand protein-Protein Interactions and Their Biological Applications, *J. Phys. Chem. C,* **2014**, 118, 28207-28219.
32. M. Valiev, E.J. Bylaska, N. Govind, K. Kowalski, T.P. Straatsma, H.J.J. van Dam, D. Wang, J. Nieplocha, E. Apra, T.L. Windus and W.A.D. Jong, NWChem: A comprehensive and scalable open-source solution for large scale molecular simulations.*Comput., Phys. Commun.,* **2010**, 181, 1477-1489.
33. L. Skripnikov, A computer program to analyse and visualise quantum-chemical calculations, 2012.
34. Y. Lee and T.G. Park, Facile Fabrication of Branched Gold Nanoparticles by Reductive Hydroxyphenol Derivatives, *Langmuir*, **2011**, 27, 2965–2971.

View Article Online
DOI: 10.1039/C6RA12076H

35. K. Pacławski, B. Streszewski, W. Jaworski, M. Luty-Blocho and K. Fitzner, Gold nanoparticles formation via gold(III) chloride complex ions reduction with glucose in the batch and in the flow microreactor systems, *Colloids Surf.A*, **2012**, 413, 208–215.
36. J. Bhaumik, N.S. Thakur, P.K. Aili, A. Ghanghoriya, A.K. Mittal and U.C. Banerjee, Bioinspired Nanotheranostic Agents: Synthesis, Surface Functionalization, and Antioxidant Potential, *ACS Biomater. Sci. Eng.*, DOI: 10.1021/ab500171a.
37. P. Mulvaney, Surface Plasmon Spectroscopy of Nanosized Metal Particles, *Langmuir* **1996**, 12, 788.
38. P. Joshi, V. Shewale and R. Pandey, Tryptophan-Gold Nanoparticle Interaction: A First-Principles Quantum Mechanical Study, *J. Phys. Chem. C,* **2011**, 115, 22818-22826.
39. W.J. Yin, X. Gu and X.G. Gong, Magic number 32 and 90 of metal clusters: A shell jellium model study, *Solid State Commun.*, **2008**, 147, 323-326.
40. M.P. Johansson, D. Sundholm and J. Vaara, Au32: A 24-Carat Golden Fullerene, *Angew. Chem. Int. Ed.*, **2004**, 43, 2678-2681.
41. Y. Khanhuathon, W. Siriangkhawut, P. Chantiratikul and K. Grudpan, Spectrophotometric method for determination of aluminium content in water and beverage samples employing flow-batch sequential injection system, *Journal of Food Composition and Analysis,* **2015**, 41, 45-53.
42. M.I.S. Verissimo and M.T.S.R. Gomes, The quality of our drinking water: Aluminium determination with an acoustic wave sensor, *Analytica Chimica Acta*, **2008**, 617, 162-166.
43. A. Saini, J. Singh, R. Kaur, N. Singh and N. Kaur, Nphthalimide-based organic nanoparticles for aluminium recognition in acidic soil and aqueous media, *New J.Chem.* **2014**, 38, 4580-4586.
44. M. Rani, L. Moudgil, B. Singh, A. Kaushal, A. Mittal, G.S.S. Saini, S.K. Tripathi, G. Singh, A. Kaura, Understanding the Mechanism of Replacement of Citrate from the Surface of Gold Nanoparticles by Amino acids: A Theoretical and Experimental Investigation and their Biological Application, *RSC Advances*, **2016**, 6, 17373-17383.
45. D. Guo, J. Wang, X. Wang, H. Luo, H. Zhang, D. Cao, L. Chen and N. Huang, Double directional adjusting estrogenic effect of naringin from Rhizoma drynariae (Gusuibu), *Journal of Ethnopharmacology*, **2011**, 138 451– 457.

View Article Online
DOI: 10.1039/C6RA12076H

Figure Caption

Figure 1: (a) UV-Visible spectra of $HAuCl_4$ +Naringin mixture in a buffer of pH = 9 with [$HAuCl_4$] = 0.4mM and [N] = 0.5mM at 40^oC. Blank means no $HAuCl_4$ is added. The inset shows the colour of N-AuNPs. Plots of (b) wavelength (c) intensity @ 525nm versus reaction time, respectively for the different mixtures keeping [$HAuCl_4$] = 0.4mM and [N] = 0.05, 0.1, 0.2, 0.5mM. Similarly plots of (d) wavelength (e) intensity @ 525nm versus reaction time, respectively for the different mixtures keeping [N] = 0.5 mM and [Au] = 0.2, 0.4, 0.6. 1.2mM, (f) Absorbance versus wavelength scans of [$HAuCl_4$] = 0.4mM and [N] = 0.05mM in a buffer of pH = 9 with respect to reaction temperature from 20^oC to 70^oC.

Figure 2: (a) TEM image and (b) corresponding particle size distribution of N-AuNPs. Blue arrow shows a thin layer coating around each NP. (c) TEM images of N-AuNPs in the presence of Al^{3+} (d) corresponding particle size distribution of N-AuNPs in the presence of Al^{3+}. The scale bar corresponds to 10nm.

Figure 3: The contour plot of (a) Highest Occupied Molecular orbital and (b) Lowest Unoccupied Molecular orbital of [$C_{10}H_7O_2$]-Au_{13} conjugate system.

View Article Online
DOI: 10.1039/C6RA12076H

Figure 4: TDDFT spectra of (a) $[C_6H_5O]^-$-Au_{13} and (b) $[C_{10}H_7O_2]$-Au_{13} conjugate systems.

Figure 5: NTOs for the excitations which make up the dominant peak in the Vis region (a) Hole part and (b) Particle part of $[C_{10}H_7O_2]$-Au_{13}. Phases of the orbitals are indicated in red and blue.

Figure 6: (a) photographs of colour change on addition of N-AuNPs solution to Al spiked water samples (b) UV-Vis spectrum of N-AuNPs as a function of various concentrations of Al^{3+} spiked in water sample, blank represents only N-AuNPs solution (c) plot of absorption ratios of A_{640}/A_{520} of N-AuNPs vs Al^{3+} concentration.

Figure 7: Effect of N-AuNPs on cell viability of cancer cells (a) MCF-7 (b) T47D (c) PC-3 and (d) MDAMB-231 with different concentrations of N-AuNPs = 30, 50 and 100 µg/ml by using MTT Assay. Data represented here is expressed as mean ± SE of at least three independent experiments. Significant differences were compared between untreated control versus N-AuNPs treatment concentrations and between individual N-AuNPs different treatments concentrations. * $p \leq 0.05$; ** $p \leq 0.01$; *** $p \leq 0.001$.

Figure 8: Effect of N-AuNPs on cell viability of cancer cells (a) MCF-7 (b) T47D (c) PC-3 and (d) MDAMB-23 with different concentrations of N-AuNPs = 30, 50 and 100 µg/ml by using Trypan Blue Exclusion Assay. The results are expressed as the percent of cell viability compared to the untreated control.

View Article Online
DOI: 10.1039/C6RA12076H

Figure 1

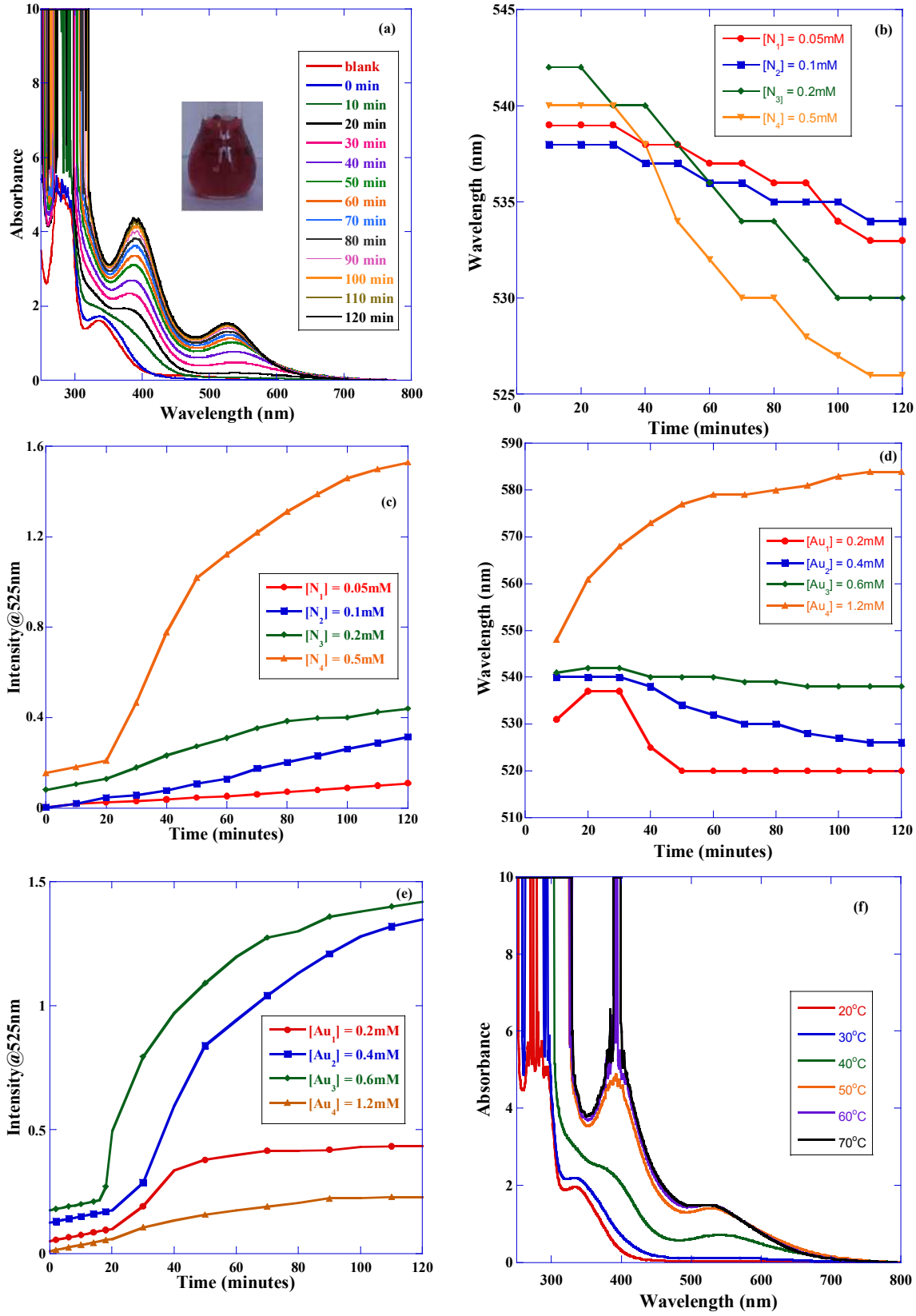

View Article Online
DOI: 10.1039/C6RA12076H

Figure 2

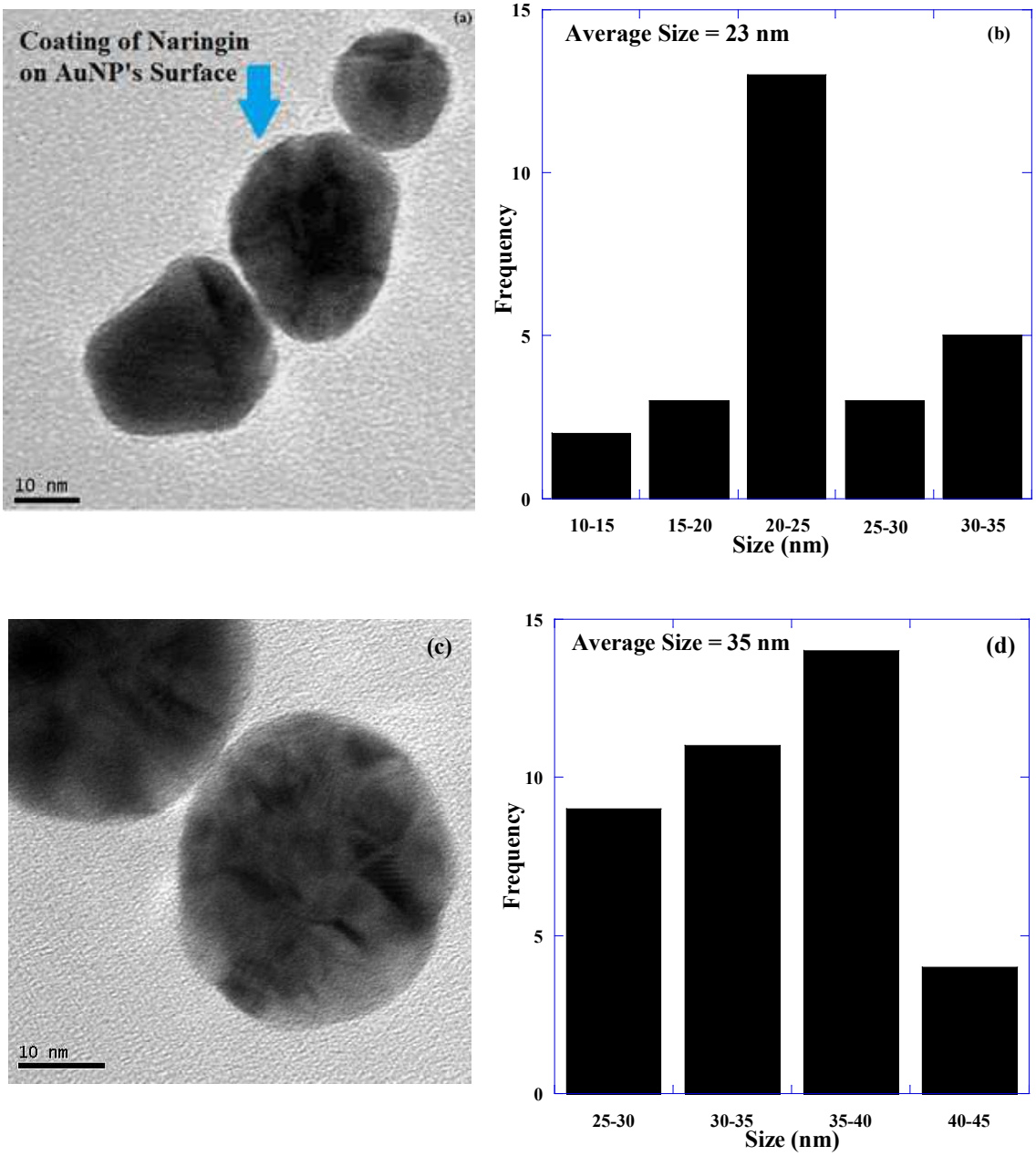

View Article Online
DOI: 10.1039/C6RA12076H

Figure 3

(a)

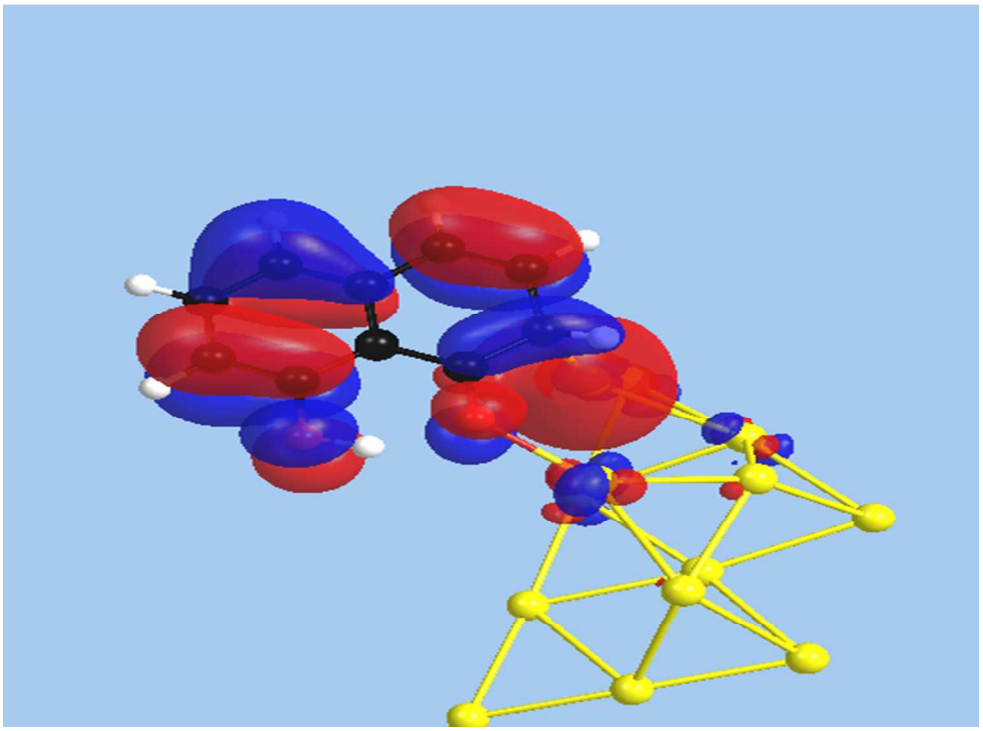

(b)

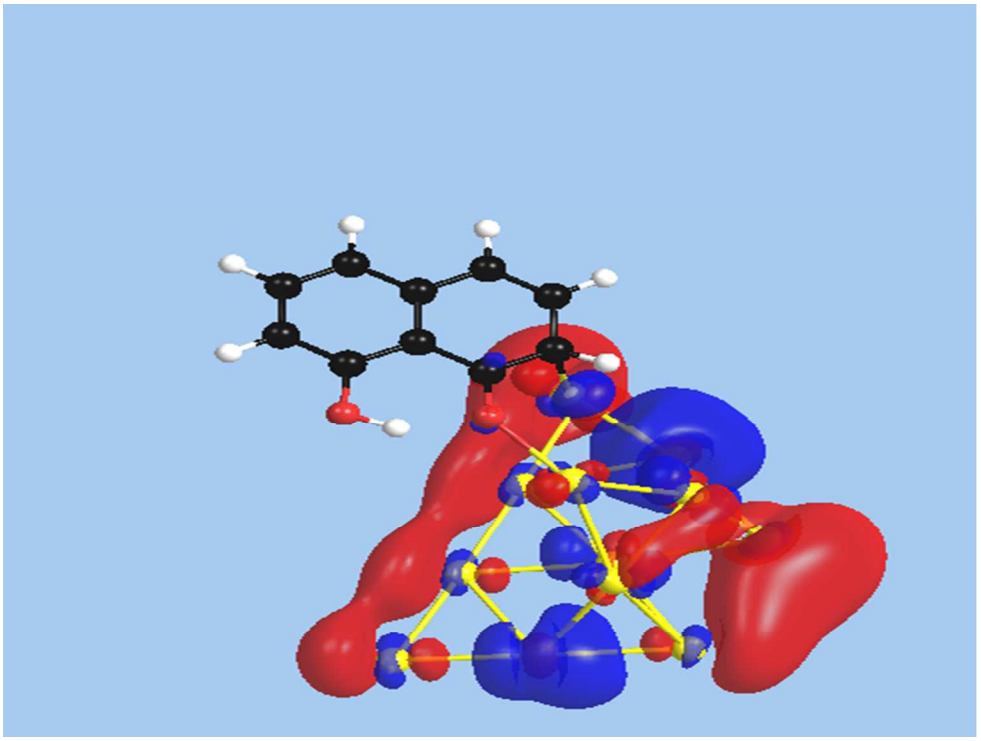

View Article Online
DOI: 10.1039/C6RA12076H

Figure 4

(a)

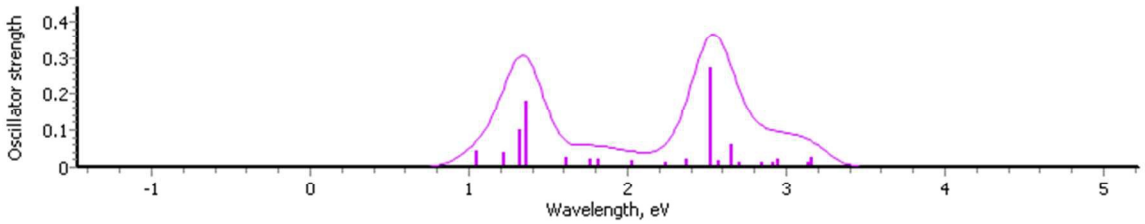

(b)

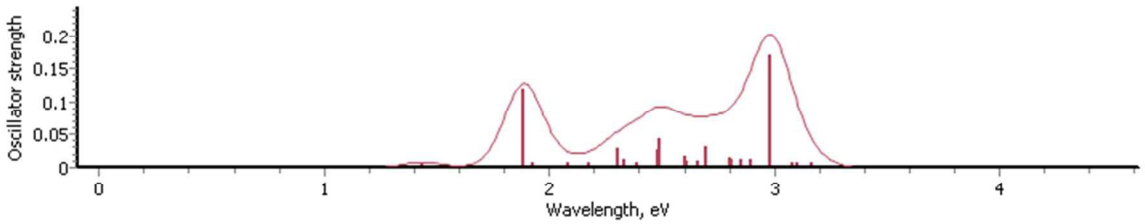

View Article Online
DOI: 10.1039/C6RA12076H

Figure 5

(a)

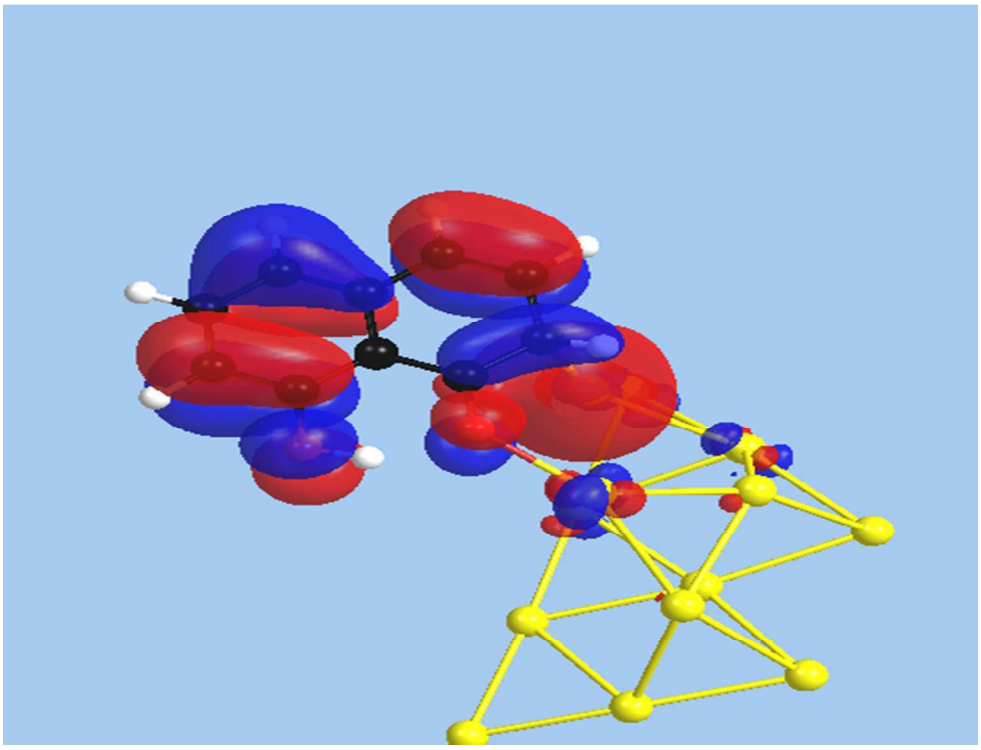

(b)

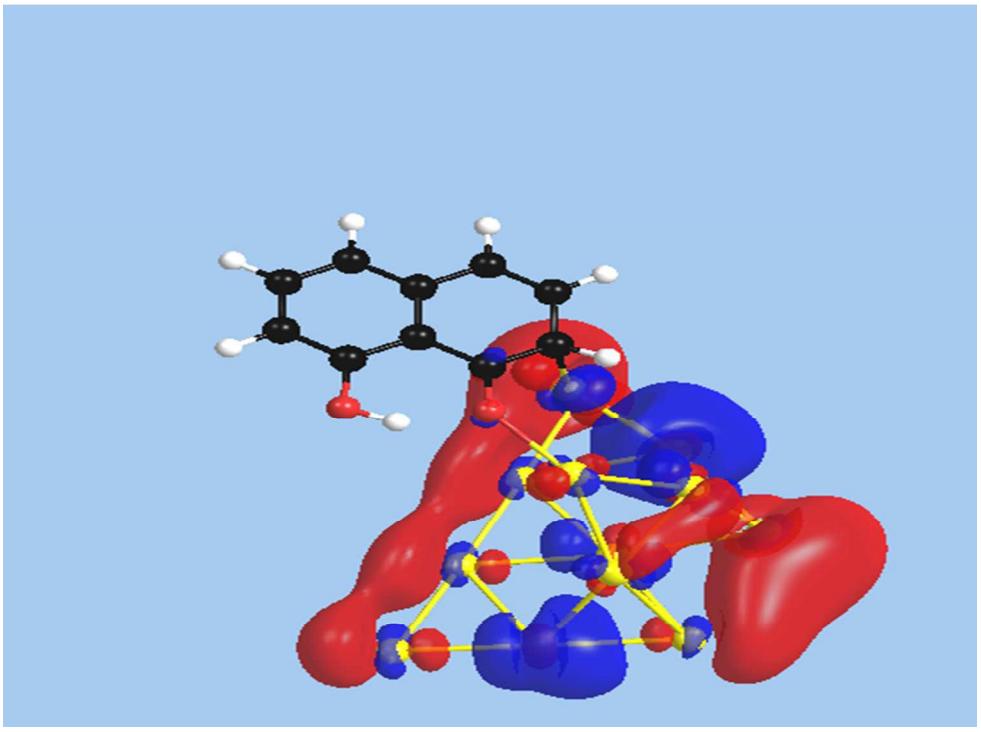

View Article Online
DOI: 10.1039/C6RA12076H

Figure 6

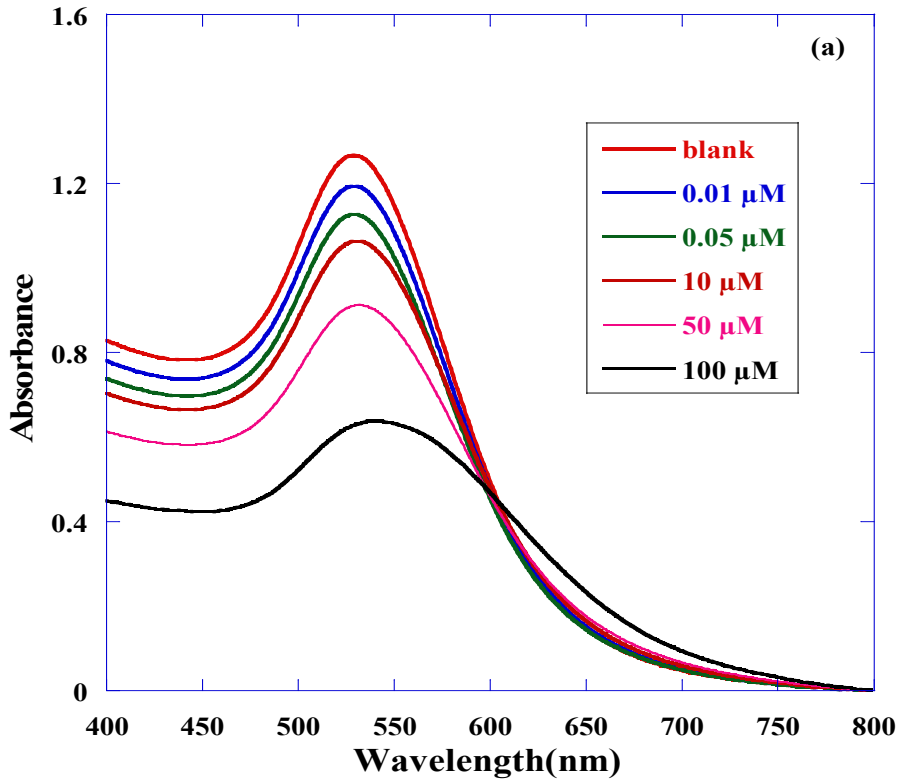

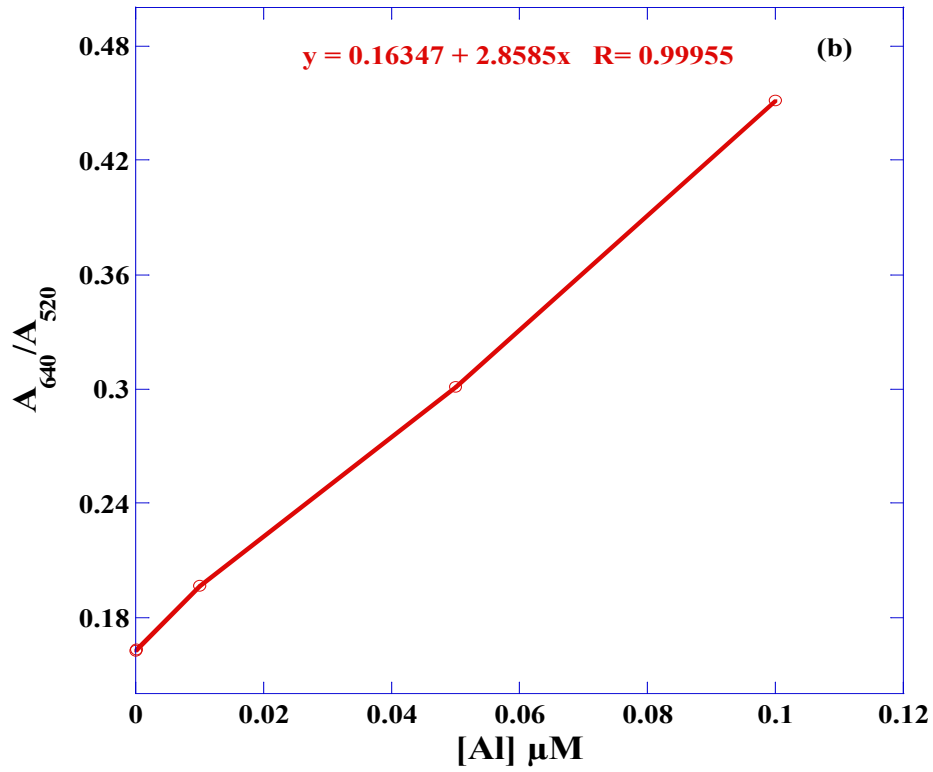

View Article Online
DOI: 10.1039/C6RA12076H

Figure 7

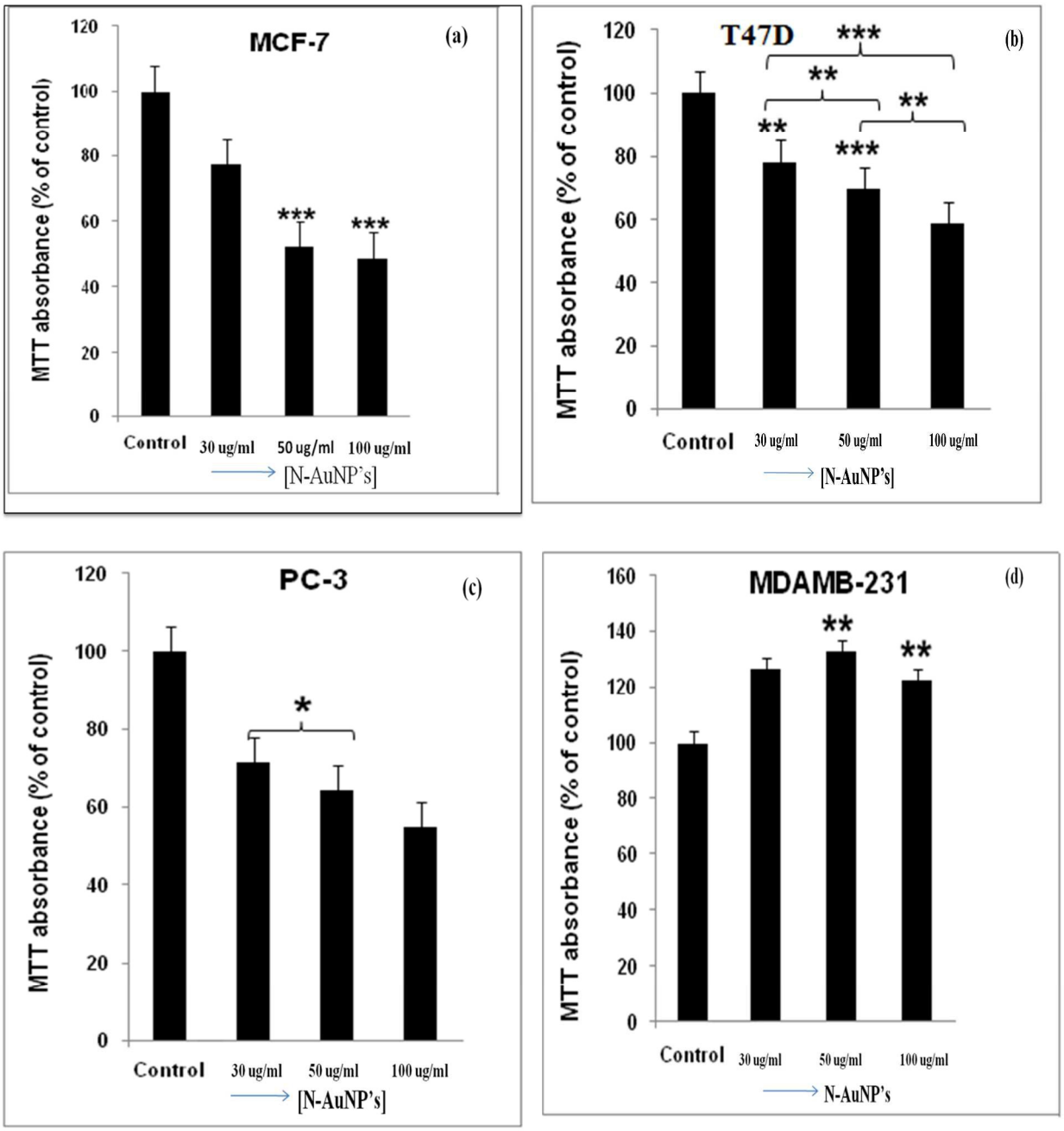

View Article Online
DOI: 10.1039/C6RA12076H

Figure 8

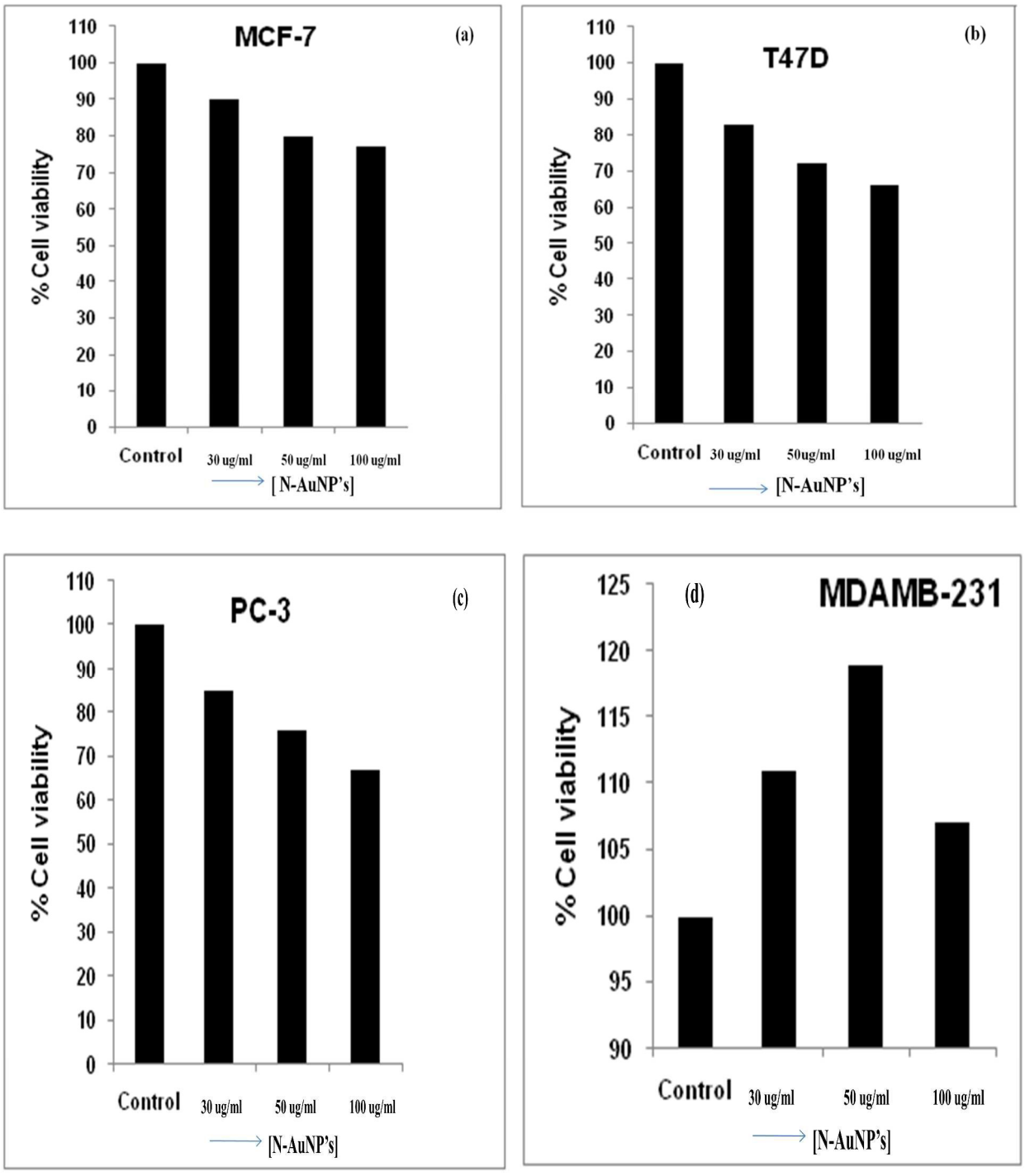

View Article Online
DOI: 10.1039/C6RA12076H

Table 1 Calculated Binding energy and Lowdin charge transfer calculations for $[C_{10}H_7O_2]$ -Au_{13} and $[C_6H_5O]^-$-Au_{13} complex system.

Structure	**BE(eV)**	**Lowdin charge/e$^-$**	
		Au_{13}	**Functional group**
$[C_{10}H_7O_2]$ -Au_{13}	2.15	-0.21	+0.21
$[C_6H_5O]^-$-Au_{13}	1.88	-0.08	+0.08

Table 2 Major contributing MO pairs (greater than 5%) to the dominant optical excitation in $[C_{10}H_7O_2]$ -Au_{13}

Initial Orbital	**Final Orbital**	**Major Transition**
155	166	d →s
153	166	d →s
158	166	p →s

Table 3 Major contributing MO pairs (greater than 5%) to the dominant optical excitation in $[C_6H_5O]^-$-Au_{13}

Initial Orbital	**Final Orbital**	**Major Transition**
143	149	d →s
141	149	d →s

Table 4 Hemolytic Analysis of N-AuNPs at various concentrations

	Absorbance @540nm				**% Hemolysis**			
N-AuNPs	25µg/ml	50µg/ml	-ve control	+ve control	25µg/ml	50µg/ml	-ve control	+ve control
	0.04	0.05	0.03	1.78	0.74%	1.19%	-----	100%

View Article Online
DOI: 10.1039/C6RA12076H

Scheme 1: A Schematic Illustration of the formation Process of Naringin stabilized Gold Nanoparticles and its interaction with Al^{3+}

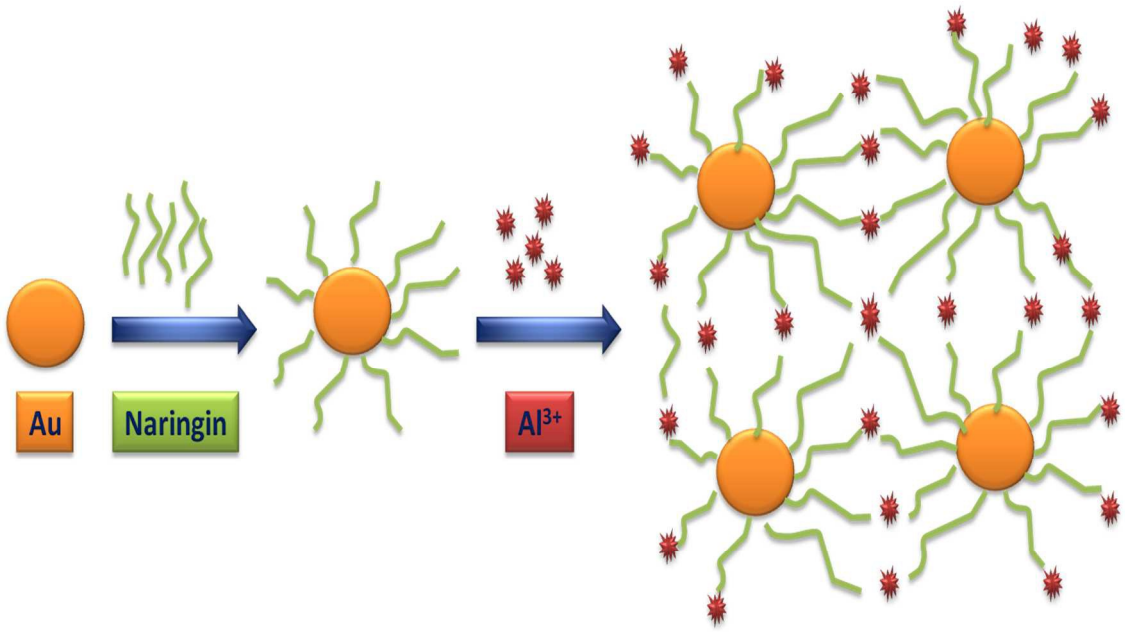

View Article Online
DOI: 10.1039/C6RA12076H